Solution combustion approach to the phase pure nanocrystalline lithium ferrite (Li$_{0.5}$Fe$_{2.5}$O$_4$) with spinel structure and magnetically soft behavior

Kirill D. Martinson[1,a], Vadim I. Popkov[1,b]

[1]Ioffe Institute, Politekhnicheskaya st., 26, Saint Petersburg, 194064, Russia

[a]martinsonkirill@mail.ru, [b]vip-07@yandex.ru

Corresponding author: K. D. Martinson, martinsonkirill@mail.ru

ABSTRACT Lithium ferrite nanoparticles (Li$_{0.5}$Fe$_{2.5}$O$_4$) were synthesized via the solution combustion method with a substantial deficiency of organic fuel (glycine, f = 0.05), followed by heat treatment of X-ray amorphous combustion products at temperatures ranging from 500 to 750 °C. Comprehensive characterization was performed using scanning electron microscopy (SEM), energy-dispersive spectroscopy (EDS), atomic absorption spectrometry (AAS), powder X-ray diffraction (XRD), and vibrating sample magnetometry (VSM). The results indicate significant morphological and structural changes in the nanopowders depending on the heat treatment temperature. Average particle sizes ranged from 14.2 to 59.5 nm, while crystallinity varied from 89.4% to 62.8%. Magnetic properties also varied, with coercivity (H_c) between 58.4 and 102.4 Oe, residual magnetization (M_r) from 5.2 to 15.4 emu/g, and saturation magnetization (M_s) from 35.1 to 60.7 emu/g. These findings demonstrate that pure lithium ferrite nanoparticles, free from impurity oxide phases, can be produced through controlled heat treatment of X-ray amorphous combustion products. Furthermore, the magnetic properties of the nanoparticles are highly sensitive to the specific heat treatment temperature, indicating that thermal processing conditions play a crucial role in determining their magnetic behavior.

1. Introduction

Spinel ferrites are a class of oxide materials known for their unique magnetic properties, which arise from their crystalline structure. These materials are characterized by the general chemical formula AFe$_2$O$_4$, where A represents metal cations (e.g., Li, Zn, Mn, Mg, Co, Ni), Fe denotes iron cations, and O represents oxygen anions. In ferrites, the cationic role is typically played by iron ions in conjunction with divalent or trivalent metals, such as zinc, magnesium, nickel, cobalt, or manganese [1–3].

The spinel crystal structure consists of a cubic close-packed arrangement of oxygen ions, with metal cations occupying interstitial sites in either tetrahedral or octahedral voids. The distribution of cations within these positions – whether normal, inverted, or random – profoundly influences the magnetic and electrical properties of the material [4]. In a normal spinel, A cations occupy tetrahedral sites, while B cations fill octahedral sites. In an inverted spinel, half of the B cations occupy tetrahedral sites, with the remaining B cations and all A cations positioned in octahedral sites [5].

The magnetic properties of spinel ferrites are primarily due to the interaction between the electron spins of cations in different coordination environments. These materials typically exhibit ferrimagnetism, where the magnetic moments of cations on distinct sublattices are oppositely aligned but do not fully cancel each other, resulting in a net magnetic moment [6]. This makes spinel ferrites invaluable in the production of magnetic cores, transformers, inductors, and other electronic components [7]. Their applications are wide-ranging and include radio electronics, telecommunications, and electrical engineering [8]. Frequently, they serve as electromagnetic wave absorbers, filters, antennas, and magnetic information carriers [9].

Among the various spinel ferrites, lithium ferrite stands out for its practical applications, particularly in microwave electronics, where it maintains a prominent position [10]. The chemical formula of lithium ferrite is typically expressed as LiFe$_5$O$_8$ or Li$_{0.5}$Fe$_{2.5}$O$_4$, depending on the stoichiometry and ionic distribution within the structure. Lithium ferrite's

structure is a variant of the spinel, featuring a cubic close-packed array of oxygen ions, with lithium and iron cations occupying the intervening spaces. Lithium cations can reside in both tetrahedral and octahedral sites, while iron cations are distributed between octahedral and tetrahedral sublattices. This distribution significantly influences the functional properties of lithium ferrite [11].

Lithium ferrite exhibits ferrimagnetic behavior, characterized by high coercivity and remanence. Its magnetic properties stem from the interaction of the magnetic moments of iron ions, which are not fully compensated due to their specific distribution within the crystal lattice. Lithium ferrite exhibits high magnetic permeability, especially at elevated frequencies, making it ideal for microwave (ultra-high frequency) applications, such as telecommunications and radar systems. High permeability allows the material to efficiently support magnetic fields, reducing energy loss in components like microwave filters and isolators [12]. Additionally, lithium ferrite's high electrical resistivity minimizes eddy current losses during high-frequency operation. Eddy currents, which cause energy dissipation as heat, are suppressed due to the material's resistivity and crystal structure, which create barriers to charge movement. This property enhances performance in devices that require efficient energy transfer and low heat generation, such as transformers and inductors [13].

Because of these properties – high magnetic permeability and low eddy current losses – lithium ferrite is widely employed in the production of antennas and electromagnetic wave absorbers. These materials enhance antenna performance and mitigate electromagnetic interference, which is crucial in densely populated radio frequency environments and wireless communication systems [14]. Multicomponent lithium ferrites, such as lithium-zinc-manganese and lithium-zinc-titanium-manganese variants, are widely used in the manufacture of microwave electronic devices [15, 16]. The advent of nanostructured material production technologies has expanded the applications of lithium ferrite nanopowders to new fields, such as sensor and detector fabrication [17], lithium-ion batteries [18], and even medical applications [19].

Numerous studies have reported the synthesis of lithium ferrite using various production methods, with the most common techniques including solid-state synthesis [20], sol-gel methods [21], solution combustion [22], and hydrothermal synthesis [23]. In recent years, the sol-gel auto-combustion method [24] and direct solution combustion methods using different organic fuels (e.g., glycine, urea, citric acid) [25–27] have been explored extensively. However, as several studies have shown [25, 26], including the author's previous work [27], the direct solution combustion method often fails to yield pure α-$Li_{0.5}Fe_{2.5}O_4$, with impurity phases such as β-$Li_{0.5}Fe_{2.5}O_4$ and γ-$Li_{0.5}Fe_{2.5}O_4$ commonly present.

This work builds upon the author's previous study [27], which employed the direct solution combustion method to synthesize lithium ferrite nanopowders. In the present study, a two-stage synthesis technique is introduced for the first time. This approach involves preparing the initial sample using the solution combustion method with a significant deficiency of glycine (f = 0.05), followed by heat treatment in the temperature range of 500–750 °C, with 50 °C increments. The choice of such a low glycine concentration was made because, under these conditions, the resulting powder is almost entirely X-ray amorphous.

2. Experimental

The following reagents were used to synthesize the initial X-ray amorphous powder: lithium nitrate ($LiNO_3 \cdot 3H_2O$, puriss., NevaReactiv), iron nitrate ($Fe(NO_3)_3 \cdot 9H_2O$, puriss., NevaReactiv), glycine (CH_2NH_2COOH, puriss., NevaReactiv), nitric acid (HNO_3, puriss., NevaReactiv), and distilled water. Lithium and iron nitrates were dissolved in 35 ml of distilled water with continuous mechanical stirring at 25 °C. After complete dissolution of the salts, 2–3 ml of 5M nitric acid and glycine were added, with glycine in a ratio of f = 0.05 relative to the stoichiometric amount. Nitric acid was included to prevent the formation of lithium and iron complex compounds. The synthesis procedure is described in more detail in [27]. The resulting solution was heated on a ceramic plate until nearly all the water evaporated, reaching the autoignition point. This process produced significant gas evolution and resulted in a solid brown product. The synthesized powder was ground mechanically in a mortar and then thermally treated in an air atmosphere for 6 hours at temperatures ranging from 500 to 750 °C, with 50 °C increments. After heat treatment, the powder was again ground mechanically and subsequently analyzed.

The chemical composition of the synthesized samples was determined using energy-dispersive spectroscopy (EDS) for iron (Fe) and oxygen (O), and atomic absorption spectroscopy (AAS) for lithium (Li), employing an Oxford INCA attachment and a Shimadzu AA-7000 atomic absorption spectrometer, respectively. The powder morphology was characterized by scanning electron microscopy (SEM) on a Tescan Vega 3 SBH microscope, and the average particle size was calculated from the micrographs using ImageJ software. X-ray diffraction (XRD) analysis was conducted using a Rigaku SmartLab 3 diffractometer with $CuK_{\alpha1}$ radiation ($\lambda = 0.154056$ nm) at 40 kV and 30 mA. Diffraction patterns were collected over a 2θ range of 20° to 80°, with a step size of 0.01° and a 3-second exposure time per step. Crystallite size distribution was evaluated using the fundamental parameter method, and the average crystallite size was estimated using the Scherrer equation. Unit cell parameters, crystallinity degree, and lattice microstrains were analyzed using Rigaku SmartLab Studio II software. Magnetic hysteresis loops (M-H) were obtained at room temperature (278 K) using a Lake Shore 7410 vibrating sample magnetometer (VSM) with an applied field up to 10 kOe. Measurements were conducted using a standard cell.

3.   Results and Discussion

The morphology of the synthesized powders was investigated using scanning electron microscopy (SEM), as shown in Fig. 1.
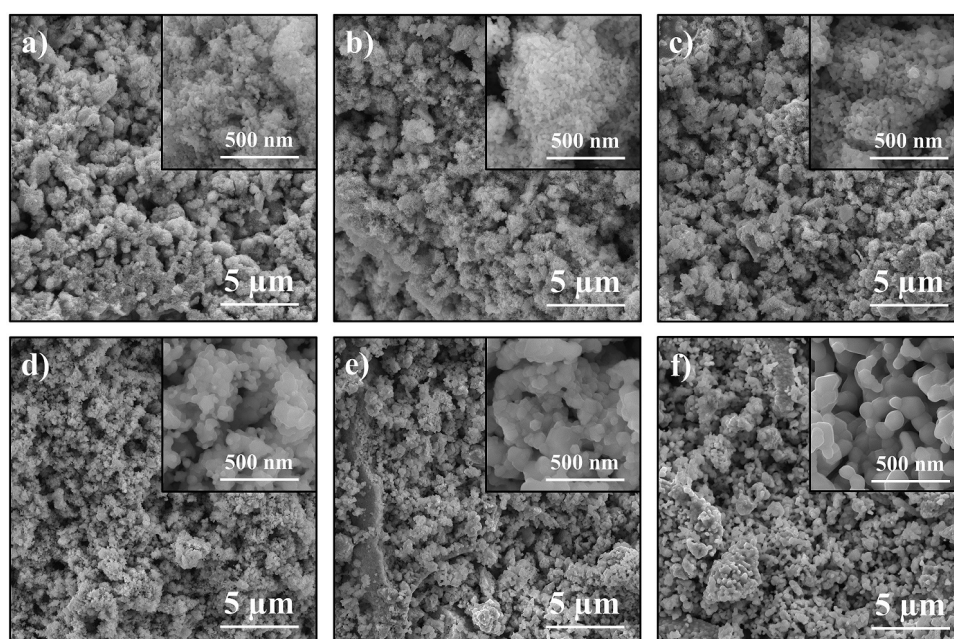

FIG. 1. SEM micrographs of α-$Li_{0.5}Fe_{2.5}O_4$ synthesized via thermal treatment of X-ray amorphous combustion products at 500 °C (a), 550 °C (b), 600 °C (c), 650 °C (d), 700 °C (e), 750 °C (f)

The SEM results demonstrate that the morphology of the lithium ferrite nanopowders depends significantly on the heat treatment temperature. All samples exhibit micron-sized clusters formed by nanoparticles, with the particle size increasing as the temperature rises. At 500 °C, the clusters appear loosely packed with weakly isolated small particles, and the surface shows noticeable porosity. Samples treated at 550 °C and 600 °C display similar features, with comparable porosity and particle size. However, at 650 °C and 700 °C, the clusters become more distinct, with clearer particle boundaries, though the surface remains loose. The 750 °C sample exhibits the most organized structure, with well-defined particle boundaries and reduced porosity. Thus, SEM analysis indicates that increasing the heat treatment temperature leads to larger particle sizes and a reduction in porosity.

To further quantify the particle size, distribution graphs were generated from the SEM images using ImageJ software (Fig. 2), with all histograms shown on the same scale for comparison. The data reveal that the average particle size increases steadily with temperature, ranging from 14.24 nm at 500 °C to 59.48 nm at 750 °C. The most significant growth occurs between 700 °C and 750 °C, where the average particle size nearly doubles, from 25.69 nm to 59.48 nm. The distributions remain monomodal across all samples, indicating a high degree of homogeneity and suggesting that particle growth occurred uniformly. This consistent growth points to the presence of an amorphous lithium ferrite phase in the initial X-ray amorphous powder, allowing direct particle growth without the formation of intermediate oxide phases. Additionally, the consistent particle growth across all samples suggests that diffusion limitations were similar at each temperature, preventing significant variations in growth rates and leading to uniform particle size increases.

The elemental composition of the synthesized samples, as determined by energy-dispersive spectroscopy (EDS) and atomic absorption spectroscopy (AAS), is summarized in Table 1. AAS confirmed the lithium content, while EDS verified the iron composition. The results indicate that the synthesized powders closely match the theoretical composition, with deviations of no more than 0.4%. Notably, these deviations increase with temperature, ranging from 0.1% at 500 °C to 0.4% at 750 °C. This increase is likely due to the volatility of lithium at higher temperatures, which can lead to lithium evaporation during heat treatment [28].

The X-ray diffraction (XRD) patterns of the initial lithium ferrite powder and the heat-treated samples are presented in Fig. 3a. The initial sample is nearly X-ray amorphous, displaying a single low-intensity amorphous halo around the 35° region. In contrast, the other samples exhibit clear diffraction peaks corresponding to the crystal planes (220), (311), (222), (400), (422), (511), and (440) of the crystalline α-$Li_{0.5}Fe_{2.5}O_4$ phase (JCPDS # 38-0259). As the processing temperature increases, a notable rise in peak intensity is observed, indicating a higher degree of crystallinity in the samples. At lower temperatures, particularly in the initial state, the diffraction peaks are less intense and more diffuse, which signifies a less ordered structure. Additionally, peak width decreases with increasing temperature, suggesting an increase in crystallite size. This observation is further supported by the shape of the crystallite size distribution, which shows a steady increase
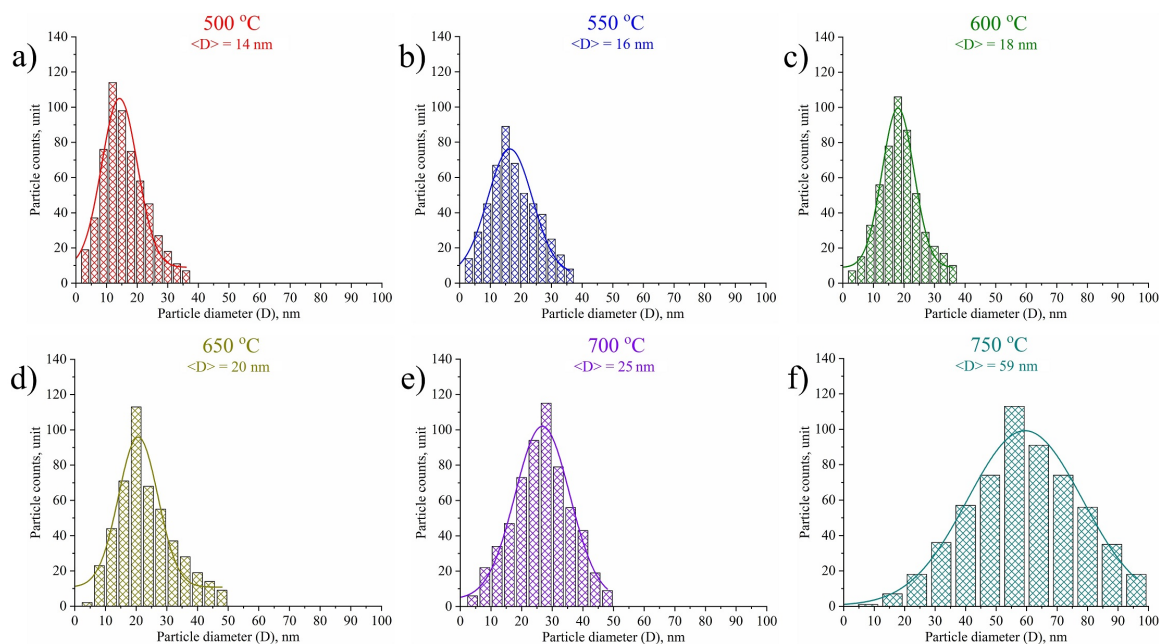
FIG. 2. Particle size distributions of lithium ferrite obtained via thermal treatment of X-ray amorphous combustion products at 500 °C (a), 550 °C (b), 600 °C (c), 650 °C (d), 700 °C (e), 750 °C (f)

TABLE 1. Elemental composition of synthesized lithium ferrite at different temperature modes

Sample	Li, at. %	Fe, at. %
500 °C	16.8	83.2
550 °C	16.8	83.2
600 °C	16.6	83.4
650 °C	16.5	83.5
700 °C	16.5	83.5
750 °C	16.4	83.6

in size with temperature (Fig. 3b). The crystallite size distribution data obtained using the fundamental parameters method align well with the visual estimates of average particle size (Fig. 2). The distributions reveal that the crystallite sizes across all samples are centered between 13±2 nm and 50±5 nm. The average crystallite size increases linearly as the processing temperature rises.

The values of the average crystallite size, degree of crystallinity, lattice parameters, and microstresses, determined using the Rigaku SmartLab Studio II software package, are shown in Fig. 4a,b. The average crystallite size was calculated using the Scherrer formula for the main crystallographic directions (220), (311), (400), (422), (511), and (440). It is evident that as the processing temperature increases from 500 °C to 750 °C, a significant rise in the average crystallite size is observed, from 10.2 nm to 49.6 nm. These results are consistent with the visual assessment of the average particle size, obtained from the micrographs (Fig. 2), and the data from the fundamental parameters method (Fig. 3b). The most pronounced increase in crystallite size occurs between 650 °C and 750 °C, suggesting an intensive crystallite growth process within this temperature range.

The degree of crystallinity was estimated using an internal standard (α-Si) with the Rietveld method, and it also increases with temperature. In the range from 500 °C to 650 °C, a moderate increase in the crystalline phase percentage is observed, but after 650 °C, the growth rate accelerates, reaching nearly 90% crystallinity at 750 °C. This high degree of crystallinity at elevated temperatures may indirectly reflect improved structural ordering of the lithium ferrite, which is further confirmed by the temperature dependence of the lattice parameters. These parameters decrease significantly, reaching values close to those reported in the literature (a = b = c = 8.324(7) Å) for the sample annealed at 750 °C [25, 27]. Hence, the reduction in lattice parameters within the 500 °C to 750 °C range may be attributed to lattice compression during crystallite growth and the corresponding increase in crystallinity.
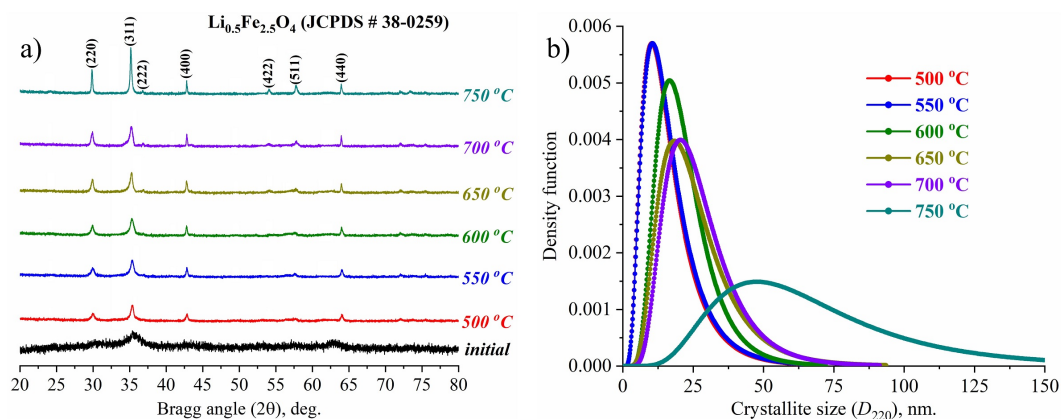
FIG. 3. Diffraction patterns (a) and crystallite size distribution (b) of α-$Li_{0.5}Fe_{2.5}O_4$ synthesized via thermal treatment of X-ray amorphous combustion products at the range of temperature from 500 to 750 °C

Microstress values also decrease notably as the temperature rises, with the most significant reduction occurring between 600 °C and 750 °C. This decline in microstresses may be linked to the relaxation of defects within the lattice at higher temperatures, coinciding with the increase in crystallinity. Therefore, the observed reduction in lattice parameters indicates a compaction of the structure, while the decreasing microstresses suggest the relaxation of internal stresses and defects.
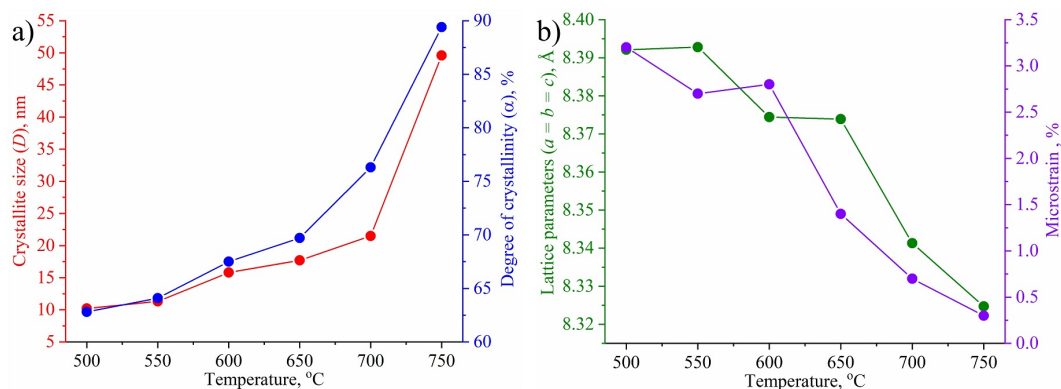

FIG. 4. Structural parameters of lithium ferrite nanopowders synthesized via thermal treatment of X-ray amorphous combustion products at the range of temperature from 500 to 750 °C
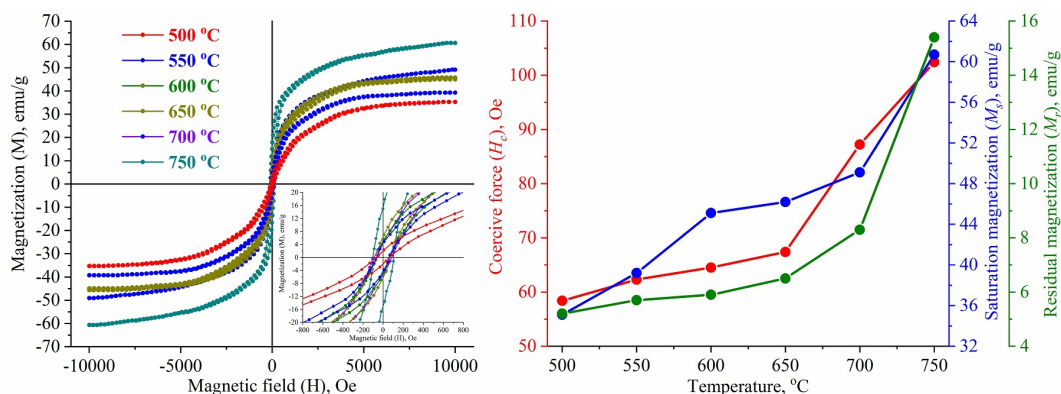

FIG. 5. M-H hysteresis loops (a) and magnetic parameters (b) of lithium ferrite nanopowders synthesized via thermal treatment of X-ray amorphous combustion products at different temperature modes

Figure 5 shows the magnetic hysteresis loops (M-H) and magnetic parameters of the lithium ferrite nanopowders (Fig. 5a,b). The hysteresis loops exhibit the characteristic shape of ferrimagnetic materials. Notably, as the temperature increases from 500 °C to 750 °C, a significant change in the loop shape is observed. At 750 °C, the hysteresis loop is the

widest, indicating higher magnetic performance, with a residual magnetization of 15.4 emu/g, saturation magnetization of 60.7 emu/g, and coercive force of 102.4 Oe. As the heat treatment temperature decreases, the loop width narrows, and both saturation magnetization and residual magnetization decline considerably. The lowest values are observed in the sample treated at 500 °C, where the coercive force, residual magnetization, and saturation magnetization are 58.4 Oe, 5.2 emu/g, and 35.1 emu/g, respectively. This behavior suggests a reduction in magnetic order at lower temperatures, likely due to thermal fluctuations that disturb magnetic domains [29, 30]. Therefore, the data clearly demonstrate that the main magnetic parameters of lithium ferrite improve with increasing heat treatment temperature, which corresponds with the observed increases in both average particle size and degree of crystallinity.

4. Conclusion

This study demonstrates the successful synthesis of the crystalline phase of α-$Li_{0.5}Fe_{2.5}O_4$ without impurity oxide phases through the heat treatment of X-ray amorphous products derived from solution combustion. The formation of lithium ferrite begins at 500 °C, and as the processing temperature increases, the average particle size grows from 14.2 nm to 59.5 nm, while the degree of crystallinity improves from 62.8% to 89.4%. The unit cell parameters change linearly with temperature, reflecting structural evolution in the samples, with the sample treated at 750 °C showing the closest match to reference values. Given that this sample also exhibits the lowest percentage of amorphous phase, the 750 °C temperature regime is deemed optimal for obtaining well-crystallized lithium ferrite. Furthermore, the key magnetic parameters – coercive force, residual magnetization, and saturation magnetization – also increase linearly with temperature, corresponding to the rise in both particle size and crystallinity.

References

[1] Salih S.J., Mahmood W.M. Review on magnetic spinel ferrite (MFe_2O_4) nanoparticles: From synthesis to application. *Heliyon*, 2023, **9**(6), P. e16601.

[2] Martinson K.D., Cherepkova I.A., Sokolov V.V. Formation of cobalt ferrite nanoparticles via glycine-nitrate combustion and their magnetic properties. *Glass Physics and Chemistry*, 2018, **44**, P. 21–25.

[3] Askarzadeh N., Shokrollahi H. A review on synthesis, characterization and properties of lithium ferrites. *Results in Chemistry*, 2024, **10**, P. 101679.

[4] Liandi A.R., Cahyana A.H., Kusumah A.J.F., Lupitasari A, Alfariza D.N., Nuraini R., Sari R.W., Kusumasari F.C. Recent trends of spinel ferrites (MFe_2O_4: Mn, Co, Ni, Cu, Zn) applications as an environmentally friendly catalyst in multicomponent reactions: A review. *Case Studies in Chemical and Environmental Engineering*, 2023, **7**, P. 100303.

[5] Martinson K.D., Panteleev I.B., Steshenko K.A., Popkov V.I., Effect of Bi_2O_3 contents on magnetic and electromagnetic properties of LiZnMn ferrite ceramics. *Journal of the European Ceramic Society*, 2022, **42**(8), P. 3463–3472.

[6] Dastjerdi O.D., Shokrollahi H., Mirshekari S. A review of synthesis, characterization, and magnetic properties of soft spinel ferrites. *Inorganic Chemistry Communications*, 2023, **153**, P. 110797.

[7] Sagayaraj R. A review on structural and magnetic properties of magnesium ferrite nanoparticles. *International Nano Letters*, 2022, **12**, P. 345–350.

[8] Harris V.G., Geiler A., Chen Y., Yoon S.D., Wu M., Yang A., Chen Z., He P., Parimi P.V., Zuo X., Patton C.E., Abe M., Acher O., Vittoria C. Recent advances in processing and applications of microwave ferrites. *Journal of Magnetism and Magnetic Materials*, 2009, **321**, P. 2035–2047.

[9] Dyachenko S.V., Martinson K.D., Cherepkova I.A., Zhernovoi A.I. Particle size, morphology, and properties of transition metal ferrospinels of the MFe_2O_4 (M = Co, Ni, Zn) type, produced by glycine-nitrate combustion. *Russian Journal of Applied Chemistry*, 2016, **89**, P. 535–539.

[10] Verma R., Thakur P., Sun A.-C. A., Thakur A. Investigation of structural, microstructural and electrical characteristics of hydrothermally synthesized $Li_{0.5-0.5x}Co_xFe_{2.5-0.5x}O_4$, ($0.0 \leq x \leq 0.4$) ferrite nanoparticles. *Physica B: Condensed Matter*, 2023, **661**, P. 414926.

[11] Malathi S., Wayessa S.G. A Study of Lithium Ferrite and Vanadium-Doped Lithium Ferrite Nanoparticles Based on the Structural, Optical, and Magnetic Properties. *Journal of Nanomaterials*, 2023, **2023**, P. 6752950.

[12] Verma V., Gairola S.P., Pandey V., Kotanala R.K., Su H. Permeability of Nb and Ta doped lithium ferrite in high frequency range. *Solid State Communications*, 2008, **148**(3-4), P. 117–121.

[13] Mazen S.A., Abu-Elsaad N.I., Structural, magnetic and electrical properties of the lithium ferrite obtained by ball milling and heat treatment. *Applied Nanoscience*, 2015, **5**, P. 105–114.

[14] Lysenko E.N., Nikolaev E.V., Vlasov V.A., Svirkov A.S., Surzhikov A.P., Sheveleva E.A., Plotnikova I.V., Artishchev S.A. Structural and Electromagnetic Properties of Lithium Ferrite Manufactured by Extrusion Printing. *Russian Physics Journal*, 2024, **67**, P. 960–965.

[15] Martinson K.D., Ivanov A.A., Panteleev I.B., Popkov V.I., Effect of sintering temperature on the synthesis of LiZnMnFe microwave ceramics with controllable electro/magnetic properties. *Ceramics International*, 2021, **47**(21), P. 0071–30081.

[16] Dasari M., Gajula G.R., Rao D.H., Chintabathini A.K., Kurimella S., Somayajula B. Lithium ferrite: the study on magnetic and complex permittivity characteristics. *Processing and Application of Ceramics*, 2017, **11**(1), P. 7–12.

[17] Rezlescu N., Doroftei C., Rezlescu E., Papa P.D. Lithium ferrite for gas sensing applications. *Sensors and Actuators B: Chemical*, 2008, **133**(2), P. 420–425.

[18] Ateia E.E., Ateia M.A., Fayed M.G., El-Hout S.I., Mohamed S.G., Arman M.M., Synthesis of nanocubic lithium cobalt ferrite toward high-performance lithium-ion battery. *Applied Physics A*, 2022, **128**, P. 483.

[19] Teixeira S.S., Graca M.P.F., Lucas J., Valente M.A., Soares P.I.P., Lanca M.C., Vieira T., Silva J.C., Borges J.P., Jinga L.I., Socol G., Salgueiro C.M., Nunes J., Costa L.C., Nanostructured $LiFe_5O_8$ by a Biogenic Method for Applications from Electronics to Medicine. *Nanomaterials*, 2021, **11**(1), P. 193.

[20] Berbenni V., Marini A., Matteazzi P., Ricceri R., Walham N.J., Solid-state formation of lithium ferrites from mechanicallyactivated Li_2CO_3-Fe_2O_3 mixtures. *Journal of European Ceramic Society*, 2003, **23**(3), P. 527–536.

[21] Ahmad M., Shahid M., Alanazi Y.M., Rehman A.U., Asif M., Dunnill C.W., Lithium ferrite ($Li_{0.5}Fe_{2.5}O_4$): synthesis, structural, morphological and magnetic evaluation for storage devices. *Journal of Materials Research and Technology*, 2022, **18**, P. 3386–3395.

[22] Venkatachalapathy R., Manoharan C., Venkateshwarlu M., Elfadeel G.A., Saddeek Y., Solution combustion route for Ni and Al co-doped lithium ferrite nanoparticles: Synthesis, the effect of doping on the structural, morphological, optical, and magnetic properties. *Ceramics International*, 2023, **49**(4), P. 6594–6607.

[23] Mohanty V., Govindaraj G., $Li_{0.5}Ce_xFe_{2.5-x}O_4$ (x = 0, 0.05): hydrothermal synthesis, electrical and magnetic properties. *Materials Research Express*, 2018, **5**, P. 055014.

[24] Fu, Y.-P., Lin C.-H., Liu C.-W., Yao Y.-D. Microwave-induced combustion synthesis of $Li_{0.5}Fe_{2.5}O_4$ powder and their characterization. *Journal of Alloys and Compounds*, 2005, **395**(1-2), P. 247–251.

[25] Naderi P., Masoudpanah S.M., Alamolhoda S. Magnetic properties of $Li_{0.5}Fe_{2.5}O_4$ nanoparticles synthesized by solution combustion method. *Applied Physics A*, 2017, **123**, P. 702.

[26] Randhawa B.S., Dosanjh H.S, Kumar N. Synthesis of lithium ferrite by precursor and combustion methods: A comparative study. *Journal of Radioanalytical and Nuclear Chemistry*, 2007, **274**, P. 581–591.

[27] Martinson K.D., Panteleev I.B., Shevchik A.P., Popkov V.I. Effect of the Red/Ox ration on the structure and magnetic behavior of $Li_{0.5}Fe_{2.5}O_4$ nanocrystals synthesized by solution combustion approach. *Letters on Materials*, 2019, **9**(4), P. 475–479.

[28] Iida Y. Evaporation of Lithium Oxide from Solid Solution of Lithium Oxide in Nickel Oxide. *Journal of American Ceramic Society*, 1960, **43**(3), P. 171–172.

[29] Jing X., Guo M., Li Z., Qin C., Chen Z., Li Z., Gong H. Study on structure and magnetic properties of rare earth doped cobalt ferrite: The influence mechanism of different substitution positions. *Ceramics International*, 2023, **49**(9), P. 14046–14056.

[30] Sun B., Ma D., Bai G., Lu X., Yang J., Wang K., Xu X., Zhai Y., Quan W., Han B. Correlating the microstructure of Mn-Zn ferrite with magnetic noise for magnetic shield applications. *Ceramics International*, 2023, **49**(8), P. 11960–11967.

Information about the authors:

Kirill D. Martinson – Ioffe Institute, Politekhnicheskaya st., 26, Saint Petersburg, 194064, Russia; ORCID 0000-0001-9313-4267; martinsonkirill@mail.ru

Vadim I. Popkov – Ioffe Institute, Politekhnicheskaya st., 26, Saint Petersburg, 194064, Russia; ORCID 0000-0002-8450-4278; vip-07@yandex.ru